Anisotropic and Heterogeneous Development of Microstructures. Combining Laboratory/Synchrotron X-rays and EBSD on a few SPD Metallic Systems

Anisotropic and Heterogeneous Development of Microstructures. Combining Laboratory/Synchrotron X-rays and EBSD on a few SPD Metallic Systems

Raúl E Bolmaro[1], Natalia S De Vincentis[1], Emanuel Benatti[1], Andrea M Kliauga[2], Martina C Avalos[1], Norbert Schell[3], Heinz-Günter Brokmeier[4].

[1] Instituto de Física Rosario-Facultad de Ciencias Exactas, Ingeniería y Agrimensura CONICET-UNR. Bv. 27 de Febrero 210 bis, (S2000EZP), Rosario, Argentina.
[2] Materials Engineering Department, São Carlos Federal University, São Carlos, Brazil.
[3] Helmholtz-Zentrum Geesthacht, GEMS Outstation, Notkestr. 85, 22607 Hamburg, Germany.
[4] Institut für Werkstoffkunde und Werkstofftechnik, TU Clausthal, Agricolastr.6, 38678 Clausthal-Zellerfeld-Helmholtz-Zentrum Geesthacht, GEMS Outstation, Notkestr. 85, 22607 Hamburg, Germany.
E-Mail: bolmaro@ifir-conicet.gov.ar

Abstract. The onset of Severe Plastic Deformation (SPD) regime is quite instructive on the possible origins of the nano-microstructures developed in metals and alloys. It is known that grain fragmentation and dislocation accumulation, among other defects, proceed at different paces depending fundamentally on grain orientations and active deformation mechanisms. There have been many attempts to characterize nano-microstructure anisotropy, leading all of them to sometimes contradictory conclusions. Moreover, the characterizations rely on different measurements techniques and pos-processing approaches, which can be observing different manifestations of the same phenomena.

On the current presentation we show a few experimental and computer pos-processing and simulation approaches, applied to some SPD/alloy systems. Williamson-Hall and Convolutional Multiple Whole Profile (CMWP) techniques will be applied to peak broadening analysis on experimental results stemming from laboratory Cu Kα X-rays, and synchrotron radiation from LNLS (Laboratório Nacional de Luz Síncrotron, Campinas, Brazil) and Petra III line (HEMS station, at DESY, Hamburg, Germany).

Taking advantage of the EBSD capability of giving information on orientational and topological characteristics of grain boundaries, microstructures, grain sizes, etc., we also performed investigations on dislocation density and Geometrically Necessary Dislocation Boundaries (GNDB) and their correlation with texture components.

Orientation dependent nano-microstructures and domain sizes are shown on the scheme of generalized pole figures and discussions provide some hints on nano-microstructure anisotropy.

Keywords: Nanostructure, SPD, Texture, Peak Broadening Analysis.

1. Introduction

Materials subject to mechanical processing accumulate energy by generating defects, such as sub-grain boundaries, Geometrically Necessary Dislocations (GND), Incidental Dislocations (ID), twins, stacking faults, etc.. It is suspected, and sometimes confirmed, that the storage of micro/nanostructural features, and their related energy accumulation, is dependent on grain orientation besides the known dependence on crystallography, alloy, strain path, etc.. However no general rules can be envisaged for energy accumulation despite the huge amount

of experimental results already available on the literature. To make the things worst, the investigations have been made by using different techniques, instruments, protocols and analysis tools. X-ray diffraction has become a standard for microstructural investigation, as well as EBSD has developed as a powerful technique for that purpose more recently. Both techniques allow to observe the same landscape with different lenses. The scale of both techniques somehow overlap and their interpretation leads alternatively to consistent or contradictory results [1-3] .

On the current Conference a set of publications show some results obtained by three different x-ray sources, laboratory x-ray machine (x-pert MPD, Cu $K\alpha_{1,2}$ radiation, x-ray lenses), synchrotron radiation at Laboratorio de Luz Sincrotron, Campinas, Brazil, and synchrotron radiation at DESY, Petra III, Hamburg, Germany [4-6]. Williamson-Hall and CMWP approaches have been used for extracting data from X-ray data about nano-microstructural defects like domain sizes, dislocation densities and twins [7-9]. Also EBSD has been applied to evaluate microstructure development. A few systems have been investigated and a few conclusions can be obtained that seems to be general, despite more investigations need to be performed.

The current work shows data and analysis dealing with massive data, obtained at HEMS line, Petra III, DESY, Germany, with the goal of understanding better nano-microstructural development during severe deformation on a few alloys [4-9]. Also EBSD scans, supporting the main conclusions of the work, are shown.

2. Experimental approach
2.1. Synchrotron radiation
Transmission synchrotron X-ray diffraction with a beam size of 100 μm x 100 μm and λ=0.14235 Å was used. A Mar345 solid state detector, set on square shaped 3450 pixels x 3450 pixels of 100 μm x 100 μm, was located at 1081 mm behind the target sample. Typical detection times were in between 20 s and 100 s. A translation-rotation stage is set as a holding device allowing the positioning and vertical axes rotation of the samples every 5°, for the determination of complete textures for each sample. Further analysis on peak profiles has been performed by a few methods (Williamson-Hall, CMWP), including the one to be presented here, based on a combination of the results obtained by Stress Tex Calculator and an extension of Williamson-Hall method [10-11].

2.2. EBSD
The samples have been inspected exhaustively by EBSD in search of microstructural features that might help on the understanding of the current results and shed light on the development of nano/microstructure developed by deformation. Many of the results are shown elsewhere on the same conference proceedings. Only the ones pertinent to the current discussion will be shown here. The materials were properly polished by 9, 6, 3 and 1 μm diamond water suspension and 30' polishing with 0.05 colloidal silica. They were subject to EBSD scans on a FEI-FEG Quanta 200 by using a TSL-EDAX EBSD system. Step size was fixed to 70 nm and typical scans comprised 10^6 points or more.

3. Materials
3.1. 70% rolled Copper and Aluminum
Commercially pure Cu and Al were rolled at room temperature in several passes until reaching 70% reduction. The samples were polished and characterized by regular laboratory X-ray diffraction (MPD Panalytical diffractometer, Cu $K\alpha_{1,2}$ radiation), textures were measured before and after rolling deformation. Starting texture is characterized in both materials by a large Cube component, typical of rolled and recrystallized materials. A complete analysis of the data by Williamson-Hall and CMWP method, together with EBSD data and GND calculation is presented elsewhere on the current conference.

3.2. F-138 stainless steel subject to rolling and ECAP deformation.
F-138 steel has been deformed by rolling until 70% reduction and by 1 and 2 passes of ECAP following route Bc. The samples were consecutively subject to measurements on a Panalytical

MPD laboratory x-ray diffractometer, synchrotron radiation at LNLS XRD-1 beam line (Campinas, Brazil) and at GEMS, Petra III, DESY (Hamburg, Germany). All beams were characterized by LaB_6 standard powder and instrument peak broadening, resulting from various effects and for the used experimental setups, were determined to be close to 0.3°, 0.1° and 0.02°, respectively. The proper treatments of the results were ensured in each case to adequately subtract the influence of the instrumental broadening. Results and details on the Williamson-Hall and CMWP analysis together with EBSD data are presented also on the current conference.

4. Synchrotron results

The current analyses of the results were carried out first using Stress Tex Calculator, software developed by C. Randau et al. [10-11], to extract texture and miscrostructural data from image plates, registering complete Debye-Scherrer diagrams in our case. The software integrates each peak, by fitting Pseudo-Voigt functions, and extracts integrated intensities and Full Width at Half Maxima (FWHM). The transformation from image plate axes system to pole figure angle system is made as described in Klein and Bunge [12]. Afterwards the intensity Pole Figures (or regular pole figures, PF) can be analyzed by any post-processing/analysis texture software (Beartex, popLA, Mtex, LaboTex, etc.). Peak broadening as a function of the sample orientation can be understood as a sort of Generalized Pole Figure (GPF), as defined long ago by H.-J. Bunge. However, whatever the mode we define peak width (FWHM, integrated peak width, etc.), despite the peak broadening stems from physical effects, it cannot be understood as a physical property. Moreover, calculating from peak width, or any of the derived physical and material characterization quantities (dislocation density, grain size, etc.) their orientation distribution, as it is made with the calculation of Orientation Distribution Functions, is not a completely solved problem.
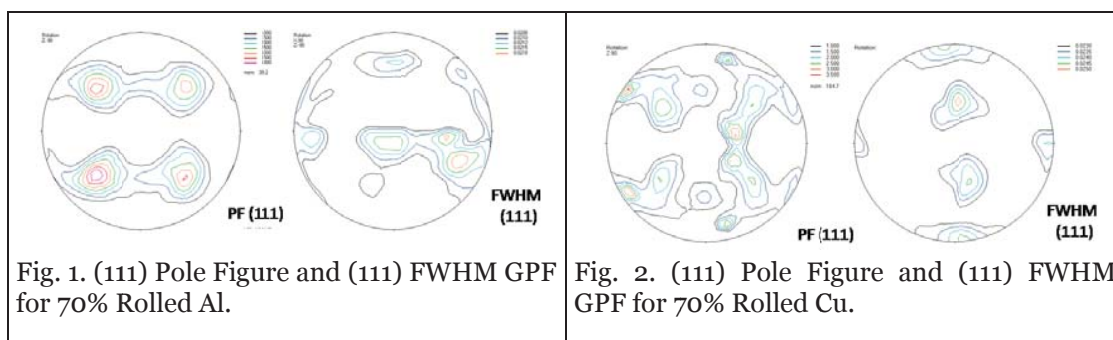

Fig. 1. (111) Pole Figure and (111) FWHM GPF for 70% Rolled Al.	Fig. 2. (111) Pole Figure and (111) FWHM GPF for 70% Rolled Cu.

Fig. 1 shows the raw results for texture, (111) PF, and FWHM GPF for rolled Al. The texture shows a preeminence of Cube component that was present on the commercial quality material that did not disappear after 70% reduction. A first striking characteristic coming up from the comparison of PF and FWHM GPF is the complementary aspect of each pair of figures: Where the PFs show maxima almost always the FWHM GPFs show minima, and vice versa. First suspicion would be that the smaller the intensity of the peaks, because of texture effects, the wider they can be just because of statistical effects. That is, if the peaks are not at least 2 or 3 times higher than the background the fitting could be not accurate enough. However, even at very low texture intensities the FWHM do not diverge uncontrollable. A few spikes, no more than a dozen on the whole set, were eliminated because they were clearly a fitting mistake because of low statistic. Moreover, if the values on the very apex of higher intensities is inspected the same behavior can be detected, with increasing FWHM with decreasing intensities. Even when the intensities are a few times random, the statistic is more than enough for fitting the peaks with low error on the lower intensity regions of the pole figures.

Fig. 2 shows similar results for rolled Cu. Cube component is also dominant and the rule of higher intensities ≡ slender peaks holds, with some overlaps that are not significant.

Fig. 3 shows results for rolled F138 steel. F138 1X and 2X ECAP samples are shown on Figs. 4 and 5. Fig 4 shows the expected texture results as (111), (200) and (220) PF, and FWHM GPF also shows the complementary behavior shown on the rest of the samples. Fig. 5 shows that after 2 passes complementary behavior starts diluting but it is still noticeable. The exceptions to the rule are the best proof that peak broadening does not come from fitting difficulties due to the low intensities. Some very low intensity directions on the PF do not show automatically an increase on FWHM. See for instance the central area of (200) PF, for which the related (200) FWHM GPF does not show any correlated broadening.
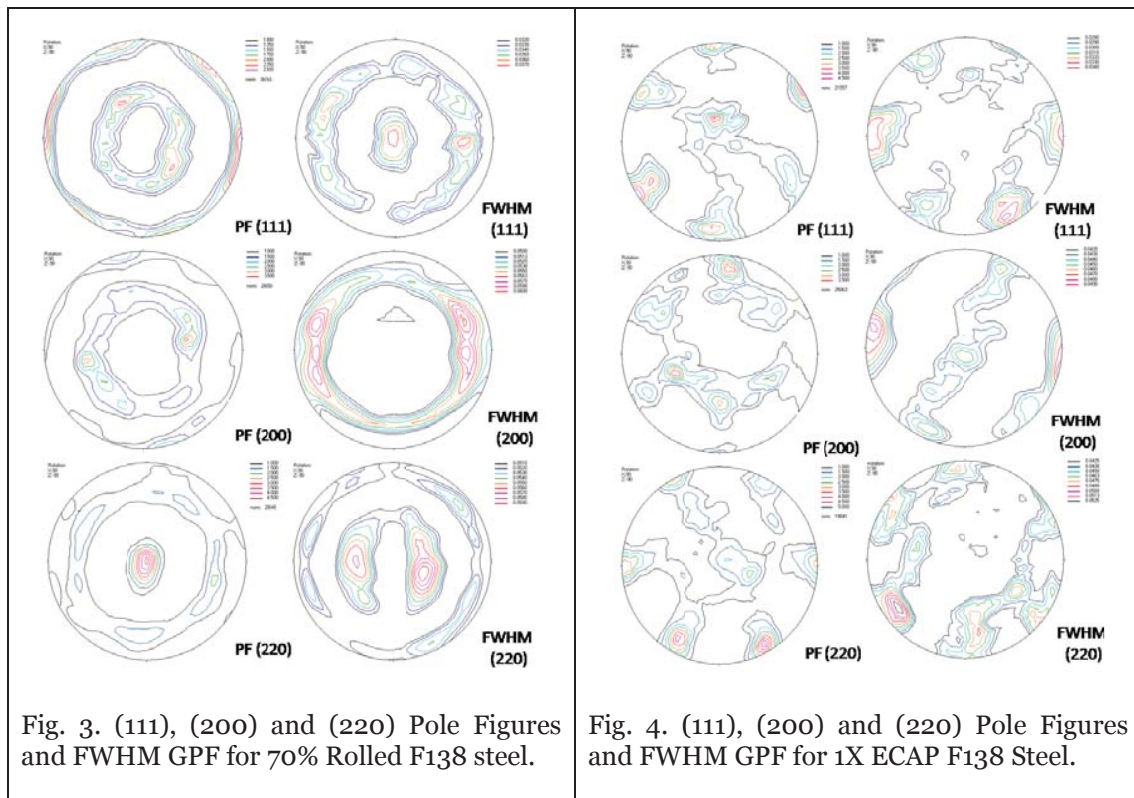

Fig. 3. (111), (200) and (220) Pole Figures and FWHM GPF for 70% Rolled F138 steel.

Fig. 4. (111), (200) and (220) Pole Figures and FWHM GPF for 1X ECAP F138 Steel.

5. Analyses

By following the modified Williamson-Hall approach the FWHM, GPFs can be analyzed as a set of diffractograms, every 5º x 5º on (α, β) coordinates, by fitting the usual equation:

$$\frac{FWHM.Cos(\theta)}{\lambda} = \frac{0.9}{D} + (\frac{\pi M^2 b^2}{2})\rho^{\frac{1}{2}}K^2 C \qquad [1]$$

where FWHM: peak width calculated by Stress Texture Calculator after subtraction of instrumental peak broadening, θ: Bragg angle, D: domain size, b: Burgers vector, M: factor characterizing the effective outer cut-off radius of dislocations, ρ: dislocation density, K: 2 sin θ/λ, C: average dislocation contrast factors. No planar defects like twins or stacking faults were considered on this first approach to the evaluation. All these concepts will be handled somehow roughly but keeping rigorousness as much as possible. For instance, M will not be evaluated but it is known that its value cannot be lower than 1 or higher than 2 for dislocation densities smaller than about $10^{14}m^{-2}$ or larger than about $5 \times 10^{15}m^{-2}$, respectively.
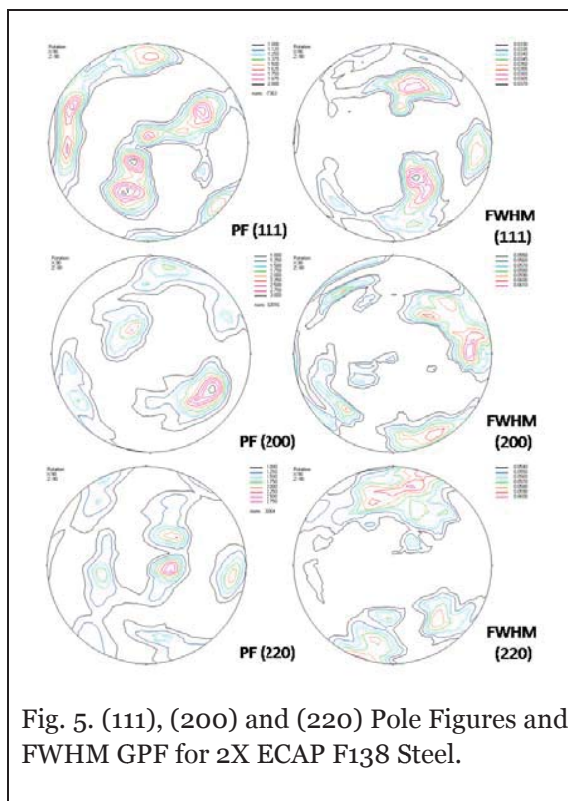
Fig. 5. (111), (200) and (220) Pole Figures and FWHM GPF for 2X ECAP F138 Steel.

Two new GPF can be obtained, dislocation density (ρ-GPF) and Domain Size (D-GPF). The equation was applied after subtracting the instrumental peak broadening, calculated from a previous measurement, on the same image plate detector, of LaB_6 NIST standard. The powder was used to fill a rectangular shape box of dimensions similar to the metallic samples.

The equation [1] was fit by a minimization routine, the whole process resulting in the determination of D and ρ as functions of (α, β). Stacking faults were not considered on the current analysis. They are shown for the F138 rolled material on Fig. 6 a-b. Domain sizes vary in between 20 nm and 45 nm and dislocation densities (multiplied by M^4, which can be assumed to be close to 1) are in between $0.5 \cdot 10^{15}$ m^{-2} and $3.5 \cdot 10^{15}$ m^{-2}.

Given the beam width (100 μm x 100 μm), the thicknesses of the samples (aprox. 1-2 mm) and the domain size (between 20 and 45 nm), the number of measured grains is in between 150 and 1500, which constitute statistically acceptable numbers for medium textured samples.
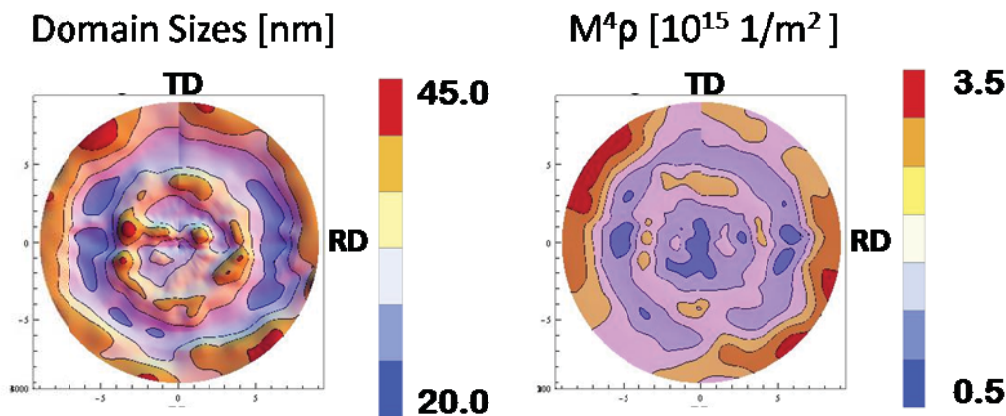

Fig. 6. a) Domain Size (D-GPF) and b) Dislocation Density (ρ-GPF) Generalized Pole Figures for 70% rolled F-138 steel.

6. EBSD results.

For reasons that will become clear on the discussion session we show EBSD scans, 70 nm steps, for the 70% rolled F138 steel as Inverse Pole Figures (IPF) maps separated in 2 partitions, one comprising only the grains with the (110) direction perpendicular to rolling plane, with a maximum misorientation of 15° from the ideal direction, and the other with the remaining crystals (Figs. 7 a-c). For each one of those partitions we calculated the Kernel Average Misorientation (KAM) distributions shown on Figs. 7 b-c). Figures 8 a-c) shows the IPF map and KAM for the same partitions ((110) directions perpendicular to the rolling plane and all the others). The discussion of the results is spared for the last session.

Figure 7 a). EBSD scan of 70% rolled F-138 steel. Step size = 70 nm, no cleaning procedure. Average CI= 0.76
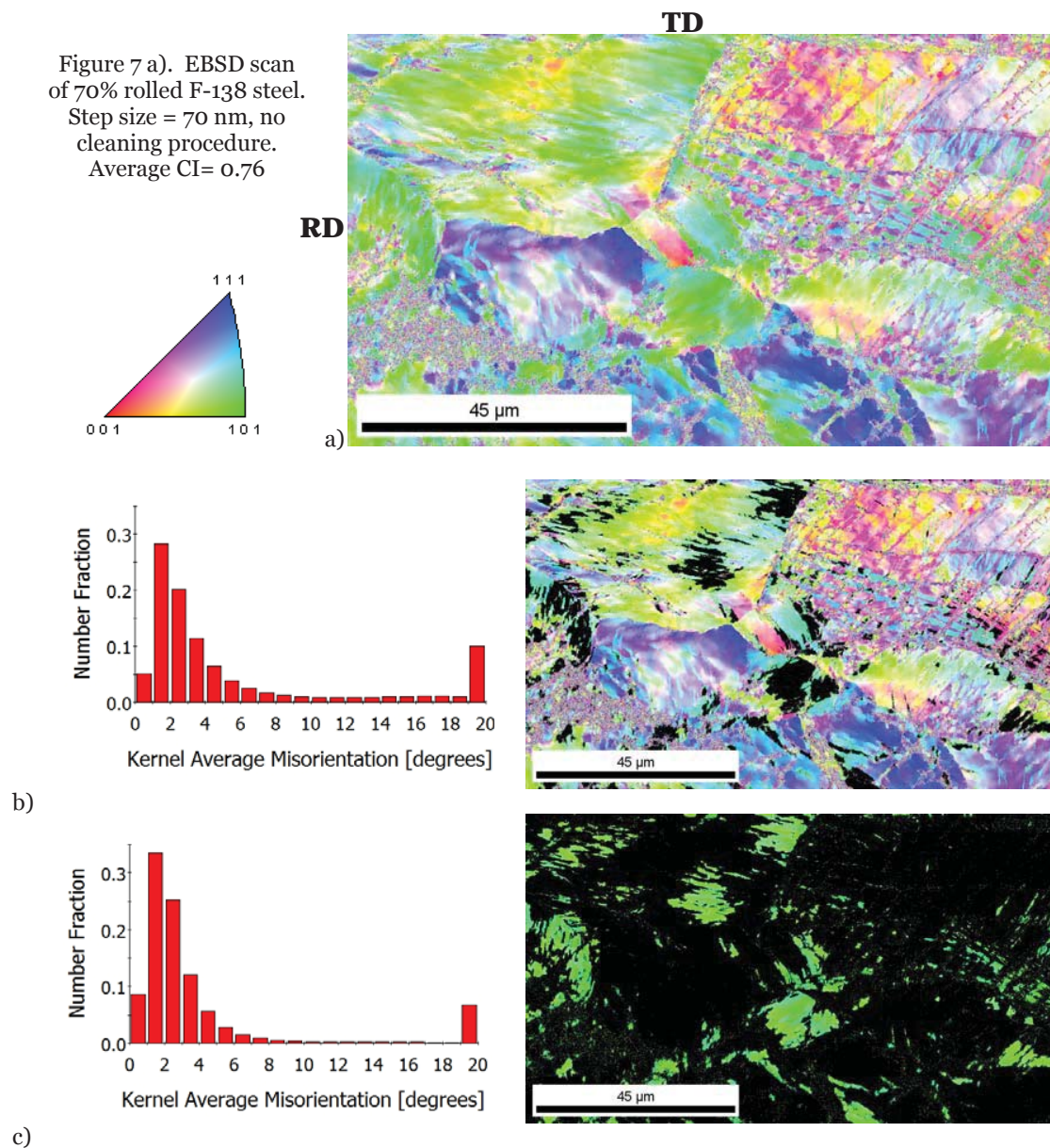

b)

c)

Figure 7. IPF and KAM calculated until the 4th neighbor for b) all directions except the ones with (110) perpendicular to the rolling plane c) only the (110) directions perpendicular to the rolling plane.

7. Discussion and conclusions

Fig. 6 shows that not always broad peaks are associated with simultaneously decreasing grain sizes and increasing dislocation densities but that the correlation is more complex and have to be analyzed by more elaborated models like the Modified W-H approach. We can see there is a trend for having the lower dislocation densities on the directions where the domain sizes are smaller, exception made for the center of the pole figures where a low dislocation density is accompanied by a moderately larger domain size. That shows that not only the peaks widen but the quality of the broadening distinguishes well between order dependent and independent effects, reflected that on the complex (α, β) variations of D and ρ. By comparison with the regular intensity PF it seems that the low dislocation density in the center of the ρ−GPF is correlated with a high intensity on the center of the (110) PF, showing a preferred (110) direction perpendicular to the rolling plane. Same correlation seems to exist

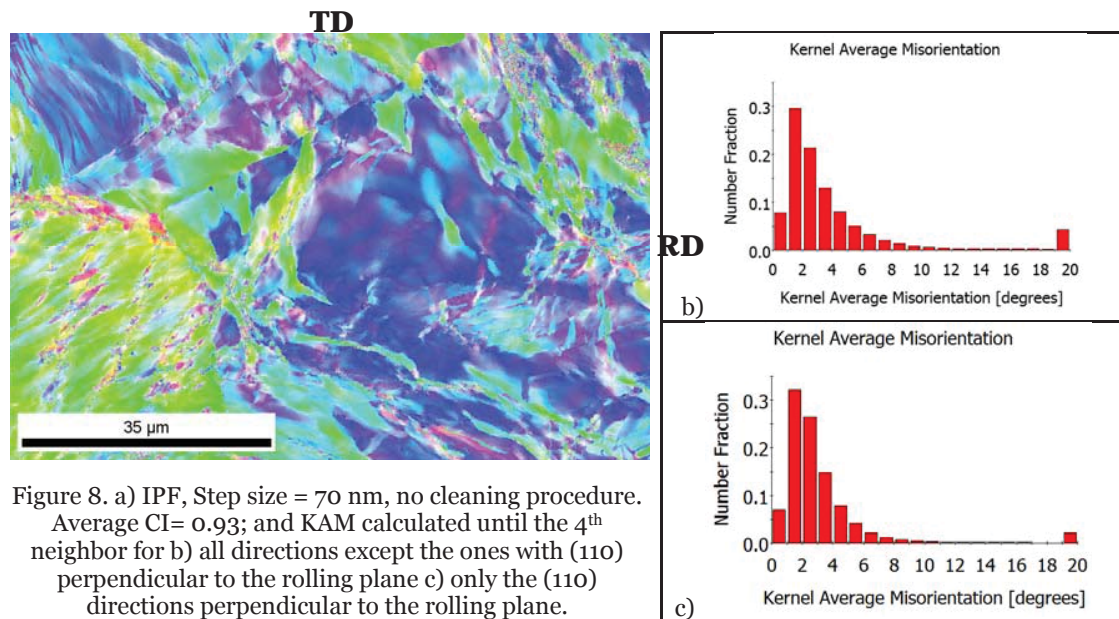between a low value on ρ–GPF in a ring at approximately 45°-50° and a similar ring shown on the (110) PF.

Figure 8. a) IPF, Step size = 70 nm, no cleaning procedure. Average CI= 0.93; and KAM calculated until the 4th neighbor for b) all directions except the ones with (110) perpendicular to the rolling plane c) only the (110) directions perpendicular to the rolling plane.

D-GPF shows large values on the RD and TD directions (in plane directions) what is compatible with the expected average sizes of the grains, elongated but fractured along RD and almost constant, although also fractured, along TD (what is called "chocolate bar" shape). This characteristic seems to be associated to macroscopic rather than to microstructural effects.

The small features showing large D dimensions on the center of the D-GPF remain to be explained but might be correlated with the low dislocation density, in the sense that, given the sensitivity of highly collimated X-rays to very low misorientations, absence of loose arrays of dislocations may also increase the measured domain size.

The lower dislocation density on the center of the ρ–GPF, apparently correlated with high population of (110) planes contained on the rolling plane (direction (110) coincident with ND) is well described by the EBSD data and KAM charts shown on Fig. 7 a-c. KAM is usually connected with the storage of defects, mainly GND and ID boundaries. The KAM for the partition showing the grains with <110> direction perpendicular to the rolling plane has a smaller average and lower standard deviation than the rest of the grains on the other partition. Similar scans and distributions for the same material heat treated during 1 h at 600 °C (Fig.8 a-c)), showed that the difference between both grain partitions starts vanishing, with the average misorientations due to dislocation arrays on the most misoriented grains converging to values similar to the <110>//ND direction. That shows that the large concentrations of dislocation arrays on the most populated directions, not in coincidence with <110>//ND, are more unstable and prone to rearrange and combine.

The smaller dislocation densities are mostly located on the sample directions in coincidence with the directions showing the smallest domain sizes, and also in coincidence with the more intense directions of some of the PF. We can only risk a model by which the more populated orientations would be composed of smaller and dislocation cleaner domains than the grains remaining on the background of the Orientation Distribution Function (ODF), which would be composed of larger domains populated by more or less loosely distributed dislocations. It seems like the dislocations on the stable texture components might be arranged in compact GND, fragmenting the grains in small domains, more or less clean of dislocations and low internal misorientations. The opposite would happen on the grains randomly oriented on the background of the ODF.

The fact that the complementary correlation between PF and FWHM GPF starts vanishing on the 2X ECAP sample can be understood as due to the strain path change imposed to the material because of the reinsertion plus the extra rotation along the longitudinal axes. The crystals are going through different strain paths and they would not store defects monotonously as in a constant strain path deformation.

It is worthy to note that the highly complex and heterogeneous nanostructure developing on F138 steel, mainly due to the high activity of twining, might help on distinguishing anisotropic behavior of defect storage. However, a careful study of peak broadening considering the presence of twining shows that the influence of stacking faults on the magnitude of FWHM is very low.

This model is schematically shown on Fig. 9. However, it should be confirmed by more experiments and simulations. Particularly, a more precise analysis of experimental data could come out from more elaborated models (e.g. CMWP). Moreover, even if it is proved correct in the current cases, it might not hold true for other symmetries, alloys or strain paths.

Small and cleaner grains on the main orientation components

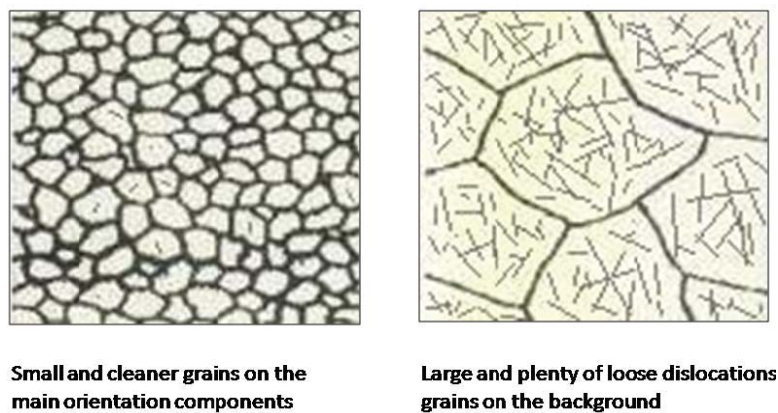Large and plenty of loose dislocations grains on the background

Figure 9. Schematic representation of the relationship between domain sizes, dislocation densities and orientations.

Micromechanically the model can be understood as it follows: a) Grains favorably oriented to be easily re-oriented to end up on the stable orientation components would go through more constant strain paths. Constant strain paths favor the appearance of stable and compact dislocation arrays and consequent grain fragmentation. b) Grains that are far from appropriate orientations would be more influenced by neighbors and suffer changes on the strain paths during the deformation process. Changing strain paths favor the formation of more unstable and less compact dislocation arrays.

However this model would assume that D and ρ are only function of the crystal orientation variables (i.e. Euler angles or Rodrigues parameters) but the high influence of sample orientation, external deformation field, sample shape, etc., all of them contained on the history of the deformation and by no means easily related with the orientation variables, might preclude the definition of a functional dependence with orientation.

Acknowledgements

References
[1] Diligent S, Gautier E, Lemoine X and Berveiller M 2001 *Acta mater.* **49** 4079.
[2] Godfrey A, Hansen N and Juul Jensen D 2007 *Metal. Mater. Trans.* **A 38** 13 2329.
[3] Li B L, Godfrey A, Liu Q 2004 *Scripta Mater.* **50** 879.

[4] Wcislak L, Schneider J R, Tschentscher Th, Klein H, Bunge H-J 2001 *Nuclear Inst. Methods Phys Res.* **A 467−468** 1257.

[5] Wenk H- R and Grigull S 2003 *J. Appl. Cryst.* **36** 1040.

[6] Brokmeier H-G, Yi S B, Schwebke B and Homeyer J 2007 *Z. Kristallogr. Suppl.* **26** 159.

[7] Williamson G and Hall W, 1953 *Acta Metall.* **1** 22.

[8] Ungár T, Gubicza J, Ribárik G, Borbély A 2001 *J. Appl. Cryst.* **34** 298.

[9] Ungár T, Dragomir I, Révész Á, Borbély A, 1999 *J. Appl. Cryst.* **32** 992.

[10] Randau C, Garbe U and Brokmeier H-G 2011 *J. Appl. Cryst.* **44** 641.

[11] Brokmeier H-G, Gan W M, Randau C, Völler M, Rebelo-Kornmeier J, Hofmann M 2011 *Nuc. Inst. & Meth. in Phys. Res.* **A 642** 87.

[12] Klein, H & Bunge H J 1999 *Z. Metallkde.* **90** 103.

[13] Littlewood P D, Britton T B, Wilkinson A J 2011 *Acta Mater.* **59** 6489.

[14] Britton T B, Wilkinson A J 2012 *Ultramicroscopy* **114** 82.

[15] Xu W, Quadir M Z and Ferry M 2009 *Met. & Mat. Trans.* **A 40** 1547.